

Supporting information: Visualizing the motion of graphene nanodrums

Dejan Davidovikj,^{*,†} Jesse J Slim,[†] Santiago J Cartamil-Bueno,[†] Herre S J van der Zant,[†] Peter G Steeneken,[†] and Warner J Venstra^{*,†,‡}

Kavli Institute of Nanoscience, Delft University of Technology, Lorentzweg 1, 2628 CJ Delft, The Netherlands, and Quantified Air, Lorentzweg 1, 2628 CJ Delft, The Netherlands

E-mail: d.davidovikj@tudelft.nl; w.j.venstra@tudelft.nl

S1. Sample fabrication

The samples are fabricated on a p-type <110> silicon wafer with a 285 nm thick layer of thermally grown silicon oxide. First, the resist is patterned using e-beam lithography. Next, layers of titanium (Ti, 5 nm) and gold-palladium (AuPd, 95 nm) are evaporated and a lift-off is performed in hot acetone. The resulting AuPd islands, shown in Figure 1a, serve as a hard mask during the reactive ion etching of SiO₂ (50 sccm CHF₃ and 2.5 sccm Ar). This step defines the cavities (Figure S1b), and as the etching stops at the silicon, a flat reflective surface is obtained that forms the fixed mirror of the interferometer. The chips are then cleaned, and graphene flakes are transferred using an all-dry transfer method, which results in the device shown in Figure S1c.

^{*}To whom correspondence should be addressed

[†]Kavli Institute of Nanoscience, Delft University of Technology, Lorentzweg 1, 2628 CJ Delft, The Netherlands

[‡]Quantified Air, Lorentzweg 1, 2628 CJ Delft, The Netherlands

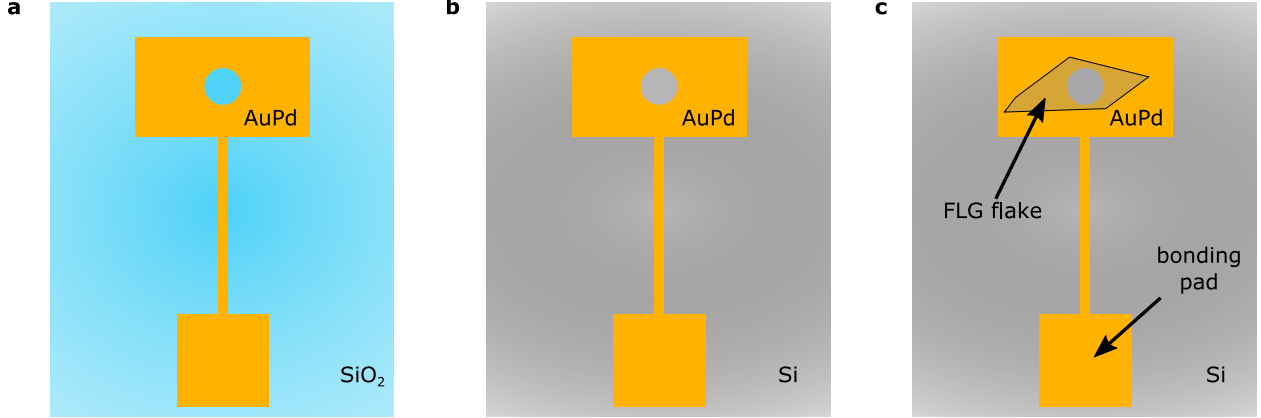


Figure S1. Sample fabrication. (a) Islands of titanium (5 nm) gold-palladium (95 nm) after e-beam patterning and lift-off. (b) The AuPd is used as a hard mask to etch the exposed SiO₂ using Reactive Ion Etching (RIE): CHF₃ (50 sccm) + Ar (2.3 sccm). (c) Graphene (or another 2-D material) is exfoliated and stamped on top of the 5 μm hole, defined by the metallic islands. Electrical contact to the nanodrum is established through the bonding pad.

S2. Optimization of the cavity depth

The cavity length is adjustable by varying the thickness of the AuPd layer, and it is chosen to maximize the responsivity at the laser wavelength for a range of graphene thicknesses as follows. The reflectivity of the device, which consists of the three interfaces schematically depicted in Figure S2b, is calculated as¹

$$R = \left| \frac{r_1 + r_2 e^{-i\delta_1} + r_3 e^{-i\delta_2} + r_1 r_2 r_3 e^{-i(\delta_1+\delta_2)}}{1 + r_1 r_2 e^{-i\delta_2} + r_1 r_3 e^{-i(\delta_1+\delta_2)} + r_2 r_3 e^{-i\delta_1}} \right|^2.$$

Here, δ_1 and δ_2 represent the acquired phase while traveling through the different media indexed in Figure S2a. Then $\delta_1 = \frac{2\pi n_1 N t_0}{\lambda}$ with N the number of layers and t_0 the thickness of a single layer, accounts for the graphene, while $\delta_2 = \frac{2\pi n_0 N z_0}{\lambda}$, with z_0 the rest position of the graphene, accounts for the cavity. The responsivity of the device, $\frac{dR}{dz}$, is plotted as a function of the cavity depth z_0 and the number of graphene layers in Figure S2b. For $z_0 = 385 \text{ nm}$ the responsivity maximizes for devices with a thickness in the range between 1 - 30 layers (0.33 - 10 nm).

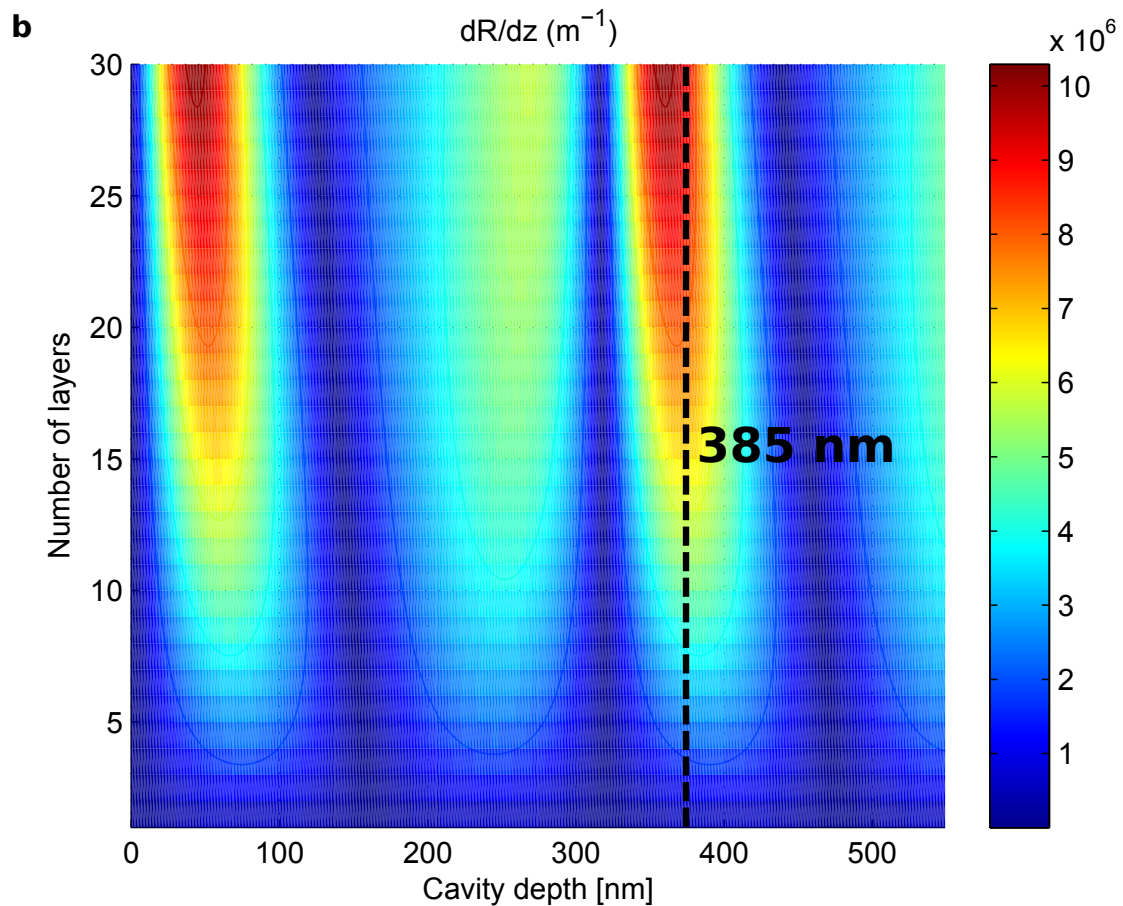
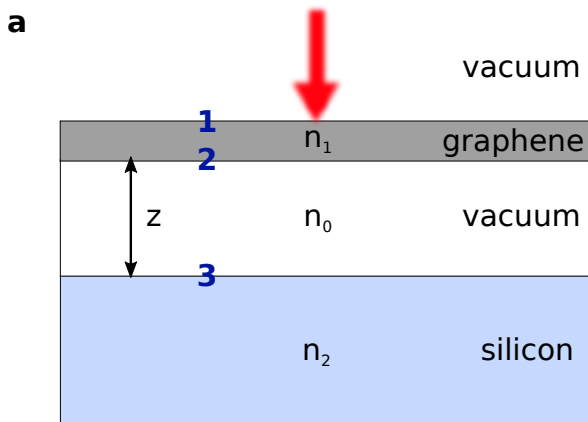


Figure S2. Calculation of the responsivity. (a) Schematic of the different media and interfaces. n_i is the refractive index of medium i ($i = 0, 1, 2$); z denotes the cavity depth and the red arrow represents the incident probe laser. (b) Calculated responsivity as a function of cavity depth and graphene thickness; the black dashed line indicates the chosen $z_0 = 385 \text{ nm}$.

S3. Optimizing the signal by electrostatic tuning

The effective spring constant of the nanodrum is adjustable by applying an electric field across the drum and the silicon substrate. Figure S3a shows spectra of the Brownian motion around the fundamental resonance mode as a function of the applied dc-voltage, V_{dc} . Two regimes are observed: for $|V_{dc}| < 1.5$ V a spring weakening is observed, which is due to the attractive electrostatic force. Larger voltages result in a significant stretching of the membrane and the increased mechanical tension gives rise to a spring stiffening behavior. The inset of Figure S3a shows the root-mean-square amplitude of the Brownian motion as a function of applied voltage. The amplitude and the signal-to-noise ratio (SNR) are maximized close to $V_{dc} = 0$, and the Brownian motion measurements discussed in the main text are performed at this setting. In the driven measurements, an alternating voltage V_{ac} is applied, and in this case, applying a dc-voltage amplifies the electrostatic driving force via $F_{ac} \propto V_{ac} V_{dc} \sin(2\pi ft)$. The amplification counteracts the reduction of the SNR due to the spring stiffening in the case $V_{ac} = 0$. Figure S3b shows the dc-voltage dependence of the resonance frequency for the driven motion. In this case, the optimum SNR is achieved at $V_{dc} = 3$ V, and this setting was chosen for the driven measurements.

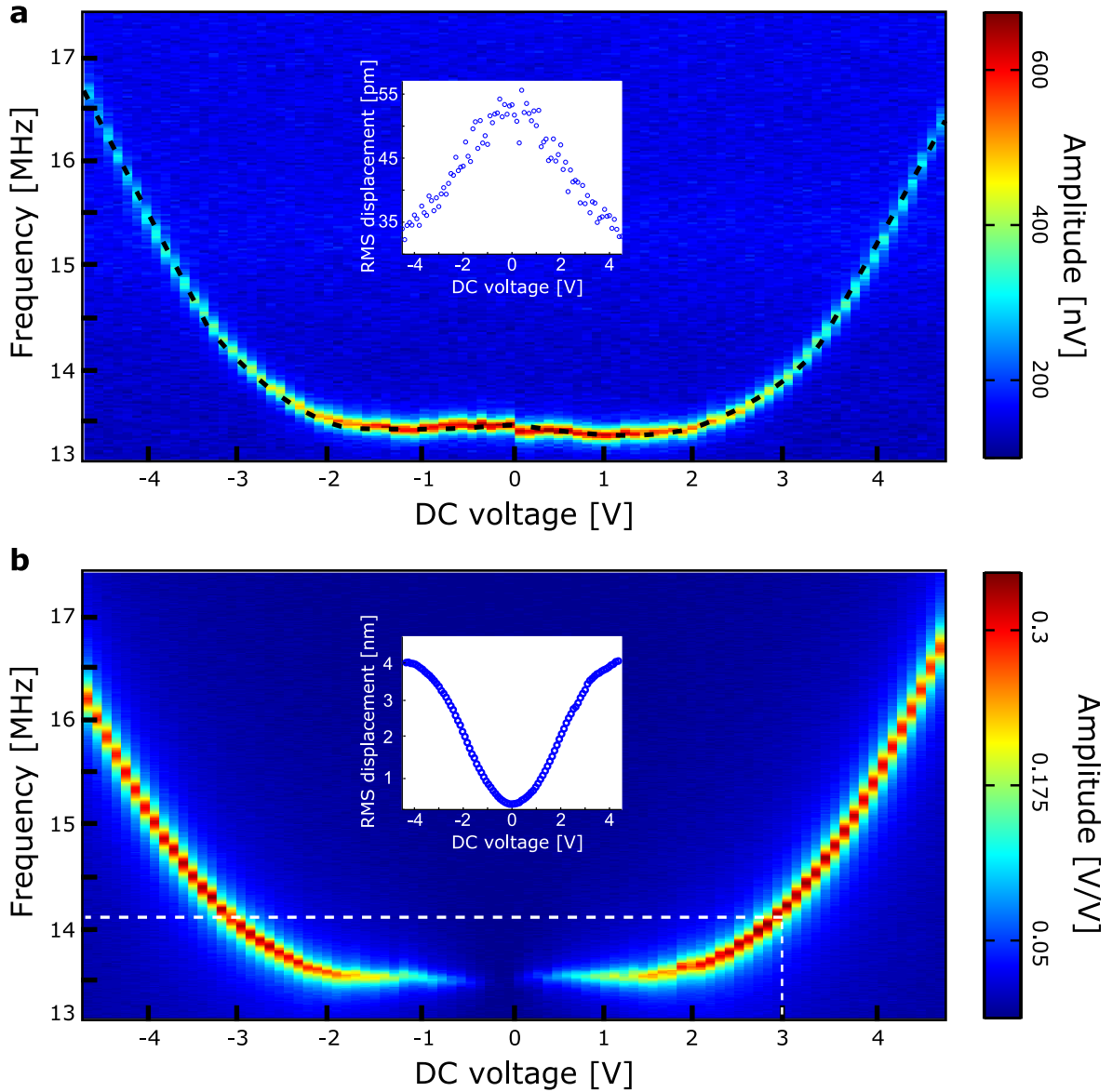


Figure S3. Electrostatic tuning of the fundamental mode. (a) Frequency response of the Brownian motion (color scale) as a function of the applied dc-voltage. The black dashed line indicates the resonance frequency. Inset: RMS amplitude of the thermal motion, showing an optimum at $V_{\text{dc}} = 0$. (b) Frequency response of the driven motion as a function of applied DC voltage. The driven motion was mapped at $V_{\text{dc}} = 3$ V, at a resonance frequency of $f_1 = 14.1$ MHz.

S4. Measuring other parameters with spatial resolution

Besides the height of the resonance peak, other characteristics can be plotted as a function of the position on the drum. For each mode and at each position, one can for instance plot the noise floor, the resonance line-width, or derived parameters such as the ratio between the resonance frequencies. Of particular interest is the spatial distribution of the resonance frequencies, which is the result of heating of the drum by the probe laser. Figure S4a shows a spatial map of resonance frequency of the driven fundamental mode, f_1 . Clearly the resonance frequency varies, with a minimum at the drum circumference and a maximum in its center. This is explained by heating of the sample by the laser: as the reflectivity of the silicon is lower than that of the AuPd, the sample heats up slightly more when probing the motion at the drum center. The thermal expansion of the substrate, together with the thermal contraction of the graphene,² induce additional tension in the membrane, which increases its resonance frequency. The resonance frequency of the drum thus maximizes when the laser hits the center of the drum. A map of the reflectivity, R , of the device, shown in Figure S4b, confirms the increased optical absorption when probing at the center of the drum.

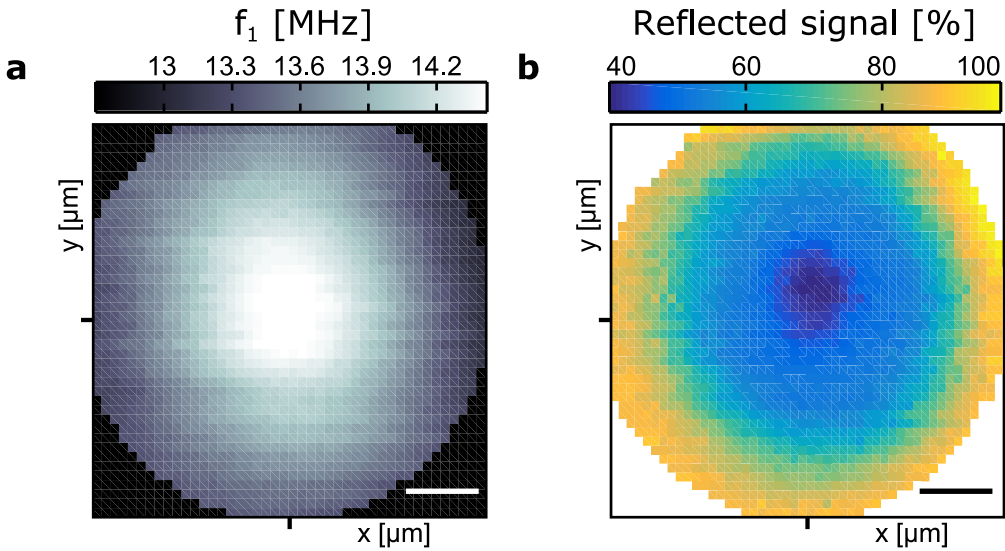


Figure S4. Spatial map of the resonance frequency of the fundamental mode. (a) Due to the different effective heating across the drum, its resonance frequency varies by 7 %. The scale bar is $1 \mu\text{m}$. (b) Reflectivity of the device, as represented by the dc output of the photodiode. The plotted signal, which is normalized to the reflectivity at the AuPd, clearly shows the increased absorption at the center of the drum.

S5. Laser power dependence and photothermal effects

Heating by the probe laser and optomechanical effects³ modify the resonance frequency and the damping of the graphene drum, and this introduces an error in the displacement calibration. To investigate these effects, we measure the non-driven spectra ($S = 2$, SA) of the fundamental mode at a laser power ranging from $0.25 - 2 \text{ mW}$. As is shown in Figure S5, a significant frequency shift is observed. All spatial maps were measured at an incident power of 0.8 mW , and by combining the frequency and reflectivity images of Figure S4a and S4b we estimate that the drum temperature is up to 3 K above the ambient temperature. The error in the displacement calibration due to laser heating is then approximately $+1\%$. Figure S5 also reveals a reduction of the Q-factor, which results from photothermal damping. The effect is not very pronounced, as the optical power is mostly absorbed by the silicon. At a laser power of 0.8 mW , the effective quality factor is reduced by approximately 6% . As the effective temperature of the mode equals $T_{\text{eff}} = \frac{TQ_{\text{eff}}}{Q}$,³ the maximum error in the displacement calibration due to photothermal damping is estimated to be -6% .

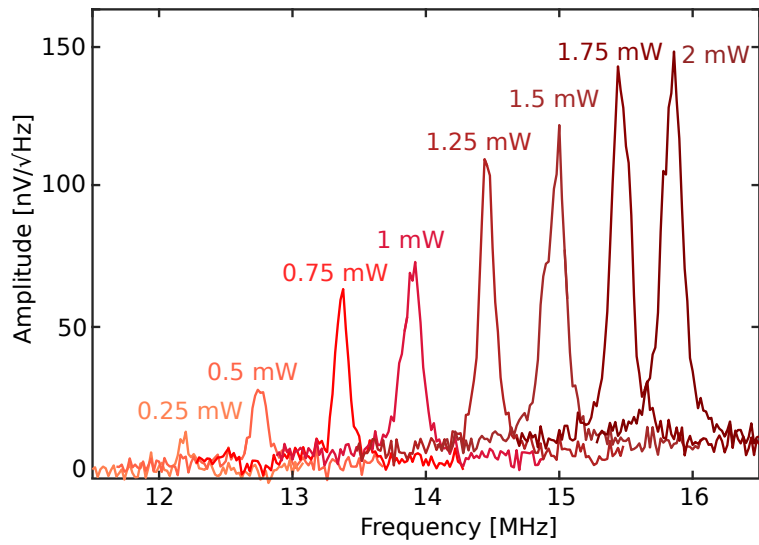


Figure S5. Laser power dependence of the Brownian motion for the fundamental resonance mode. Spectra of the non-driven motion plotted as a function of incident laser power. The combined effects of laser heating and photothermal damping cause a significant increase of the resonance frequency and a slight decrease of the Q-factor with increasing laser power.

S6. Peak-force Atomic Force Microscopy of the nanodrum surface

To investigate the origin of the distortion of the higher order mode shapes, the local stiffness of the drum was mapped using Peak-Force Atomic force Microscopy (PF-AFM). Figure S6a shows the maximum displacement at each point of the drum using 5 nN as a setpoint for the PF-AFM. It reveals a wrinkle-like feature, which is indicated by the black dashed line. From the force-displacement curves, the effective spring constant at every point is extracted and shown in Figure S6b. It reveals that the wrinkle manifests as a source of uniaxial tension along its direction, denoted by F_T . To qualitatively understand how this feature affects the mode shapes, we simulated the mode shapes using a finite element model (FEM). The location of the wrinkle is included by imposing a clamped boundary condition, along which a non-uniform tension is applied. As shown in Figure S6c, the wrinkle not only breaks the degeneracy of modes (1, 1), (2, 1), and (1, 2), but it also defines the direction of the nodal lines for the higher mode shapes. Taking the feature into account, the simulated mode shapes more closely resemble the measured ones, and they explain the unusual shapes of mode f_6 , which loses its radial symmetry, and mode f_5 which shows merging of two anti-nodes along the diameter of the drum. The resonance frequencies, which are plotted as dashed blue lines in Figure S6d, are in good agreement with the measurements, except for mode 5.

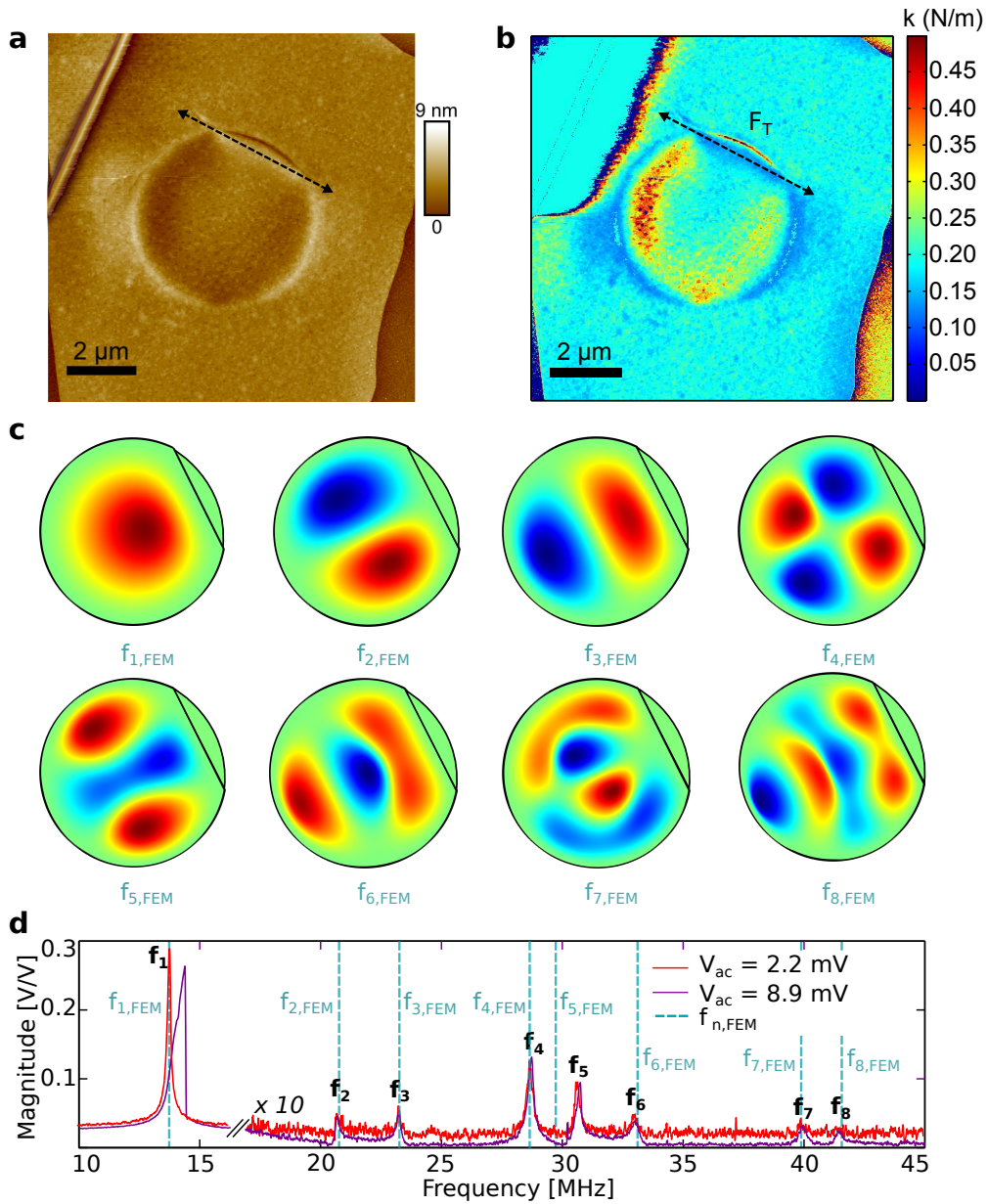


Figure S6. Effect of local stiffness variations on the mode pattern. (a) Maximum displacement at a peak force of 5 nN. The AFM scan reveals a wrinkle indicated by the dashed line. (b) Effective local linear spring constant, k , as calculated by taking the derivative of the force with respect to deflection for small deflections. (c) Simulated mode shapes when assuming a tensile force F_T along the wrinkle, indicated by the dashed line in panel (a). The simulated modes are labeled $f_{n,\text{FEM}}$, where n is the position of the peak in the frequency spectrum. (d) Simulated resonance frequencies (dashed blue lines) superimposed on the frequency response measurement of Figure 1a, main text.

S7. Measurements on additional devices

With the measurement conditions described in the Methods section, measurements were performed on two additional devices. Device 2, with a diameter of $5\text{ }\mu\text{m}$ and a thickness of 4.5 nm (13-14 layers), is shown in Figure S7a. A driven measurement reveals the four resonance modes indexed A-D in Figure S7b. The corresponding displacement profiles, shown in Figure S7c, illustrate that mode A corresponds to the fundamental mode. While from the resonance frequency of mode B a (1, 1) mode is expected, with $f_B/f_A \approx 1.6$ for a perfect membrane, the spatial image reveals a much more complicated displacement pattern. The irregular topography of the drum, displayed in the AFM image of Figure S7a, gives rise to a distorted mode pattern.

Device 3 is a single-layer graphene drum with a diameter of $5\text{ }\mu\text{m}$. Figure S8a shows an optical microscope topview and a Raman microscopy spectrum, with the pronounced 2D peak characteristic of a single layer. Figure S8b shows the measured frequency response (magnitude only) of the fundamental mode. The corresponding displacement profile is shown in Figure S8c. As in the device in the main text and in device 2 discussed above, the irregular profile may be the result of non-uniform tension or the presence of a microscopic wrinkle. As the responsivity of the interferometer reduces for thinner (low-reflectivity) devices, higher modes could not be detected for this single-layer device. Optimization of the cavity depth for single-layer graphene would enable the visualization of higher resonance modes.

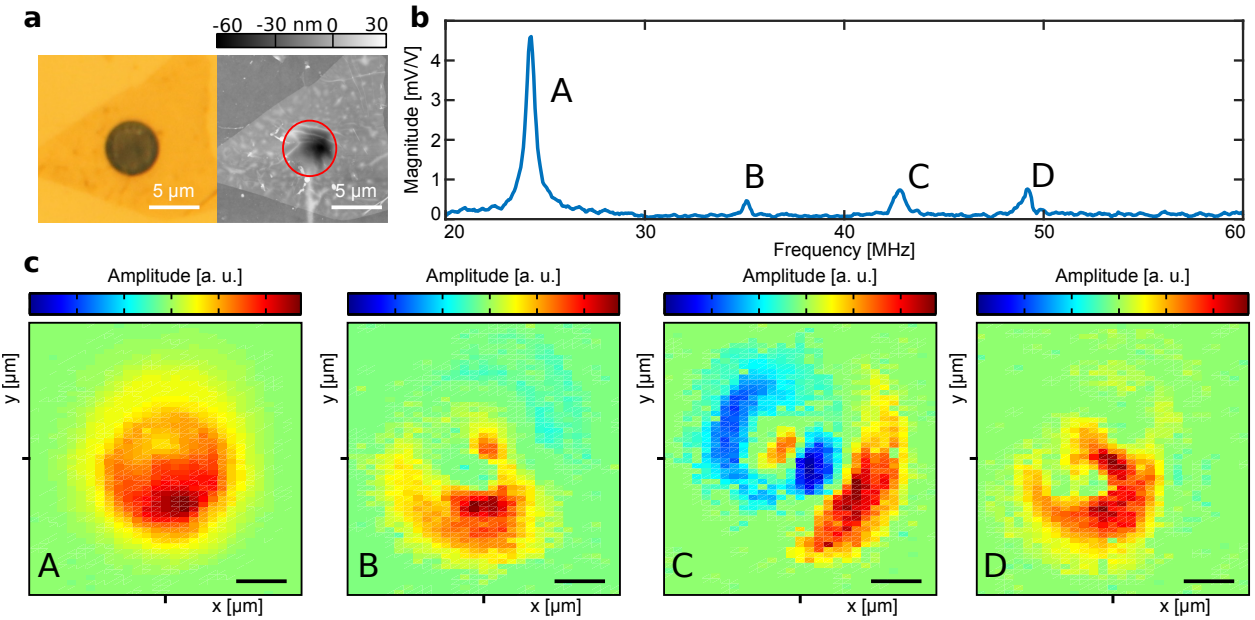


Figure S7. Device 2: 13-layer graphene. (a) Optical image (left) and AFM scan (right) of device 2. The AFM measurement shows a thickness of 4.5 nm. (b) Frequency response when driven at $V_{ac} = 8.9$ mV and $V_{dc} = 3$ V, revealing four resonance peaks labeled A-D. (c) Visualization of the displacement profiles that correspond to peaks A-D.

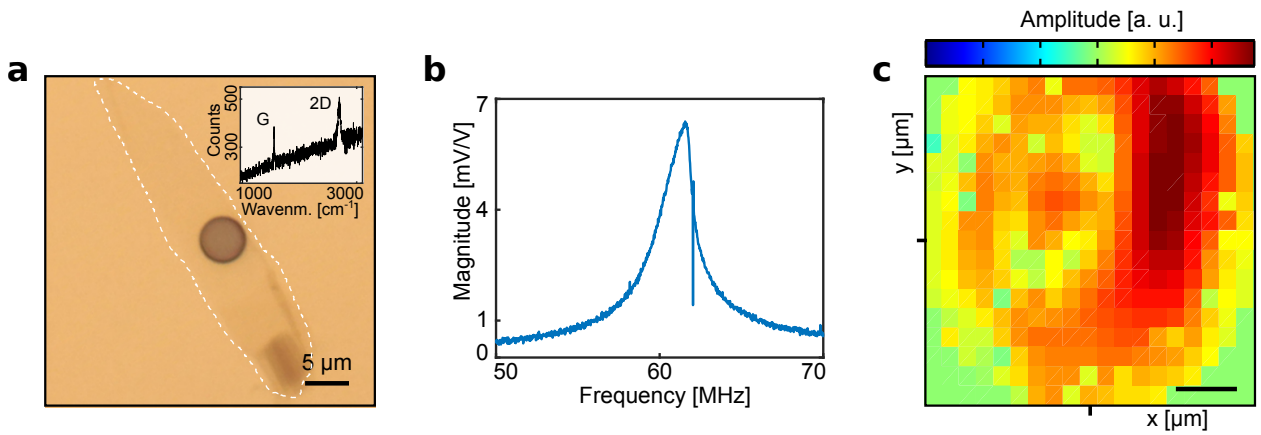


Figure S8. Device 3: Single-layer graphene. (a) Optical image of device 3. Inset: Raman spectrum taken at the drum center. (b) Driven frequency response at fundamental resonance mode, with $V_{ac} = 70$ mV. (c) Visualized displacement profile of the fundamental mode of the single-layer graphene drum.

References

- (1) Blake, P.; Hill, E. W.; Castro Neto, A. H.; Novoselov, K. S.; Jiang, D.; Yang, R.; Booth, T. J.; Geim, A. K. *Applied Physics Letters* **2007**, *91*.
- (2) Yoon, D.; Son, Y.-W.; Cheong, H. *Nano Letters* **2011**, *11*, 3227–3231.
- (3) Barton, R. A.; Storch, I. R.; Adiga, V. P.; Sakakibara, R.; Cipriany, B. R.; Ilic, B.; Wang, S. P.; Ong, P.; McEuen, P. L.; Parpia, J. M.; Craighead, H. G. *Nano Letters* **2012**, *12*, 4681–4686.